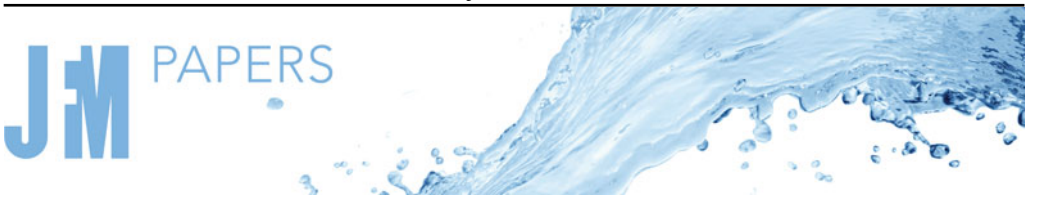
J. Fluid Mech. (2025), *vol.* 1024, A13, doi:10.1017/jfm.2025.10760



A universal criterion for underwater gas bubble stability

Yaolei Xiang[1,2], **Shenglin Huang**[1], **Xu Zhou**[1], **Pengyu Lv**[3], **Gang Wang**[1], **Tian-Yun Huang**[3], **Hongyuan Li**[1,2], **Yahui Xue**[4] and **Huiling Duan**[1,2]

[1]State Key Laboratory for Turbulence and Complex Systems, Department of Mechanics and Engineering Science, College of Engineering, Peking University, Beijing 100871, PR China

[2]CAPT, HEDPS and IFSA Collaborative Innovation Center of MoE, Peking University, Beijing 100871, PR China

[3]Department of Advanced Manufacturing and Robotics, College of Engineering, Peking University, Beijing 100871, PR China

[4]Department of Mechanics and Aerospace Engineering & Center for Complex Flows and Soft Matter Research, Southern University of Science and Technology, Shenzhen 518055, PR China

Corresponding author: Huiling Duan, hlduan@pku.edu.cn

(Received 16 April 2025; revised 14 August 2025; accepted 20 September 2025)

The stability of underwater bubbles is important to many natural phenomena and industrial applications. Since stability analyses are complex and influenced by numerous factors, they are often performed on a case-specific basis, with most being qualitative. In this work, we propose a unified and quantitative criterion for evaluating bubble stability by analysing its free energy. This criterion is broadly applicable across various bubble sizes (from nanometres to macroscale) and contact conditions (suspended, attached and trapped bubbles) on surfaces with diverse chemical (hydrophilic and hydrophobic) and morphological (flat and structured solid surfaces) features. This criterion not only applies to the classical stable bubble mode, which depends on contact line pinning at the tips of surface structures, but also predicts a new mode where the synergy between the geometry and wettability of the sidewalls maintains the bubble's stable state. The contact line can spontaneously adjust its position on the solid surface to maintain pressure balance, which enhances bubble adaptability to environmental changes. A geometric standard for solid surfaces supporting this new stable state is raised, following which we realise the optimisation of solid surface geometries to control the stability of gas bubbles. This work not only provides a universal framework for understanding underwater bubble stability, but also opens avenues for applications.

Key words: thin films, wetting and wicking, contact lines

© The Author(s), 2025. Published by Cambridge University Press.

https://doi.org/10.1017/jfm.2025.10760 Published online by Cambridge University Press

1. Introduction

Underwater gas bubbles, including suspended, attached and trapped bubbles (figure 1*a*), are widespread in nature and play important roles in various engineering applications, such as heat transfer (Jones, Evans & Galvin 1999; Guichet, Almahmoud & Jouhara 2019; Pfeiffer *et al.* 2022), underwater machinery (Arndt 1981; Versluis *et al.* 2000; Adamkowski, Henke & Lewandowski 2016), the chemical industry (Liu *et al.* 2021), and biotechnology (Prentice *et al.* 2005; Wang *et al.* 2018; Li *et al.* 2022). Sometimes, these bubbles and gas layers are desired to be long-lived because of their advantages, such as drag reduction (Granick, Zhu & Lee 2003; Choi & Kim 2006; Srinivasan *et al.* 2015; Temprano-Coleto *et al.* 2023), while in other cases, they are undesired due to disadvantages such as cavitation erosion (Karimi & Martin 1986; Adamkowski *et al.* 2016; Sun *et al.* 2025). Therefore, understanding their stability and developing effective regulation methods is important.

The analysis of underwater bubble stability encompasses the gas and liquid phases, along with their interface, which allows dissolved gas exchange (Plesset & Sadhal 1982; Xue *et al.* 2016; Tan, An & Ohl 2021). The analysis typically involves two steps. First, there are two equilibrium conditions. (i) There should be mechanical equilibrium among the hydrostatic pressure, the air pressure inside the gas layers, and the Laplace pressure of the liquid–gas interface (Atchley & Prosperetti 1989; Jones *et al.* 1999; Chappell & Payne 2007; Xue *et al.* 2016; Xiang *et al.* 2017, 2020). That is described by the Laplace equation, i.e. $p_G - p_L = \gamma_{LG}\kappa$, where p_G and p_L are the gas and liquid pressures, respectively, and γ_{LG} and κ are the surface tension and curvature of the liquid–gas interface, respectively. (ii) There should be diffusion equilibrium between the gas dissolved in the surrounding water and the gas in the air bubbles (Zhang *et al.* 2013; Lv *et al.* 2014; Xu, Sun & Kim 2014; Lohse & Zhang 2015*b*; Xue *et al.* 2016; Xiang *et al.* 2017). That is described by $p_G = sp_L$, where s is the dissolved gas saturation degree in the liquid. Second, once these equilibrium conditions are met, the stability of the equilibrium point must be analysed – specifically, whether it can persist under small disturbances. This analysis is complex as it depends on numerous factors, including water pressure, dissolved gas saturation in water, bubble size, wettability and morphology of the solid surfaces, as well as the potential pinning effect on solid surfaces (Zhang *et al.* 2013; Lv *et al.* 2014; Xu *et al.* 2014; Lohse & Zhang 2015*b*; Xue *et al.* 2016; Xiang *et al.* 2017; Tan *et al.* 2021). Currently, the stability of underwater bubbles and gas layers is assessed on a case-by-case basis, and most analyses are qualitative. A unified, quantitative standard is needed to evaluate bubble stability.

In this study, we analyse the free energy of underwater bubbles to propose a universal framework and establish a criterion for assessing their stability. This criterion is validated under a wide range of conditions, including various bubble sizes and contact conditions on surfaces with diverse chemical and morphological features. Our findings show that the criterion applies to both the classical stable bubble mode, which depends on contact line pinning, and a newly predicted mode where contact lines can move on solid surfaces. In this new mode, the combined effect of sidewall geometry and surface wettability maintains bubble stability. We further propose a geometric standard for solid surfaces that supports this new mode, and demonstrate how bubble stability can be controlled by optimising surface geometry.

2. Criterion for underwater gas bubble stability

The thermodynamic analysis states that stable submerged bubbles (including suspended, attached and trapped bubbles) can be found by minimising the total free energy. Here, we

https://doi.org/10.1017/jfm.2025.10760 Published online by Cambridge University Press

construct a free energy framework for underwater bubble systems, and derive a stability criterion based on free energy analysis. The validity of this criterion is then tested under various environmental conditions.

2.1. *Theoretical framework and derivation of the criterion*

Consider an underwater system with dissolvable gas bubbles, bulk water and a solid surface. Ignoring the influence of water vapour and temperature change, the evolution of the underwater liquid–gas interface consists of two major mechanisms: the dynamic process related to the mechanical force balance on the liquid–gas interface and the contact line, and the chemical balance related to the gas diffusion across the liquid–gas interface. This evolution can be analysed by minimising the total free energy (F_t) of the underwater system, which is written as (Xiang *et al.* 2017)

$$F_t = F_b + F_s + F_d + F_0. \tag{2.1}$$

Here, $F_b = (p_L - p_G)V_G$ is the bulk energy for the gas bubble replacing the liquid, where V_G is the volume of the air layer. Also, $F_s = \gamma_{LG}(A_{LG} + A_{SG}\cos\theta_Y)$ represents the energy of the liquid–gas interface, where θ_Y is Young's contact angle, and A_{LG} and A_{SG} are the liquid–gas and solid–gas interface areas, respectively ($A_{SG} = 0$ for suspended bubbles); and $F_d = n_G RT\ \ln[p_G/(sp_L)]$ is the excess chemical potential of the free gas in the bubble relative to that of the gas dissolved in the surrounding bulk water, where n_G is the gas mole number, R is the universal gas constant, and T is the ambient temperature. The last term, F_0, is a constant that represents the free energy of the fully wetted state.

Consider an arbitrary morphology perturbation on the liquid–gas interface together with a perturbation on the gas mole number (δn_G). Under such a perturbation, the changes of V_G, A_{LG} and A_{SG} can be found by following geometric relations $\delta V_G = \int_{\Sigma_{LG}} \delta x_N\ \mathrm{d}S$, $\delta A_{LG} = \int_{\Sigma_{LG}} \kappa\ \delta x_N\ \mathrm{d}S - \oint_{\Gamma} \delta x_{tl}\cos\theta\ \mathrm{d}l$ and $\delta A_{SG} = \oint_{\Gamma} \delta x_{tl}\ \mathrm{d}l$. Here, κ is the curvature (twice the mean curvature) of the liquid–gas interface, with a positive value when it protrudes towards the liquid, θ is the contact angle, δx_N represents the normal displacement of the liquid–gas interface Σ_{LG}, and δx_{tl} is the displacement of the contact line $\Gamma = \partial\Sigma_{LG}$ along the liquid–solid interface. Therefore, the first-order variation of the total free energy can be expressed as

$$\begin{aligned}\delta F_t = &\int_{\Sigma_{LG}} (p_L - p_G + \gamma_{LG}\kappa)\,\delta x_N\ \mathrm{d}S \\ &+ \gamma_{LG}\oint_{\Gamma} \delta x_{tl}\,(\cos\theta_Y - \cos\theta)\ \mathrm{d}l + RT\ln\frac{p_G}{sp_L}\delta n_G.\end{aligned} \tag{2.2}$$

By setting (2.2) to zero for arbitrary perturbation, three equations can be obtained naturally: $p_G - p_L = \gamma_{LG}\kappa$, $\Theta = \Theta_Y$ and $p_G = sp_L$ (Xiang *et al.* 2017). These equations describe the pressure balance across the liquid–gas interface (Laplace equation), the force balance of the contact line, and the diffusion (or partial pressure) balance between the gas bubble and dissolved gas, respectively. The diffusion equilibrium condition $p_G = sp_L$ can be also be explained by Henry's law: when the gas concentration at the bubble surface equals the far-field gas concentration, there is no net diffusion across the interface (Lohse & Zhang 2015*a*; Zhang & Lohse 2023). Furthermore, when the mechanical equilibrium and the diffusion balance are achieved simultaneously, the interface morphology should satisfy the relation $\gamma_{LG}\kappa = (s-1)p_L$. This equilibrium condition can also be verified from the perspective of gas and mass transport dynamics. The gas and mass transport process follows the diffusion equation (Lv *et al.* 2014; Lohse & Zhang 2015*b*), i.e. $\mathrm{d}[(\gamma_{LG}\kappa + p_L)V_G]/\mathrm{d}t = -A_{LG}D_G[\gamma_{LG}\kappa + p_L - sp_L]/(lK_G)$, which

https://doi.org/10.1017/jfm.2025.10760 Published online by Cambridge University Press

governs the rate of gas exchange across the liquid–gas interface. Here, l is the diffusion length, and D_G and K_G are the diffusive coefficient and Henry's constant. When the system reaches equilibrium $\gamma_{LG}\kappa = (s-1)p_L$, the diffusion equation simplifies to $\mathrm{d}[(\gamma_{LG}\kappa + p_L)V_G]/\mathrm{d}t = 0$, indicating that the net mass transfer between the bubble and the surrounding liquid ceases. This confirms that the material exchange has reached a balanced state, fully consistent with the derived equilibrium condition.

While setting the first-order variance of total free energy to zero ($\delta F_t = 0$) leads to the equilibrium state, it can be a minimum, a maximum or a saddle point of the free energy. A stable equilibrium state requires the second-order variance of the free energy to be positive for any perturbation, i.e. $\delta^2 F_t > 0$. A general stability analysis for bubble morphology perturbation together with the perturbation δn_G on an arbitrary surface is mathematically hard to discuss. However, since the gas diffusion is usually slow compared to liquid–gas interface dynamics in practice, we can decouple the evolution of the underwater gas bubble into two processes, i.e. a quick dynamic process with a sudden geometrical response of the gas bubble under hydrostatic pressures, followed by a slow chemical process with a gradual morphology evolution governed by the gas diffusion across the liquid–gas interface. In such a way, the stability analysis is also separated into two parts: the stability of the mechanical equilibrium and that of the chemical equilibrium.

First, we consider the mechanical process with no gas diffusion across the liquid–gas interface. For simplicity, we assume that the meniscus curvature κ is uniformly distributed on the liquid–gas interface (but can vary with time), and the contact angle θ always equals Young's contact angle θ_Y. Then for a given gas mole number n_G, (2.2) can be simplified as $\delta F_t = (p_L - p_G + \gamma_{LG}\kappa)\,\mathrm{d}V_G$. From this equation, we can easily find the mechanical stability criterion by setting the second-order derivative of total free energy regarding gas bubble volume to positive:

$$\left(\frac{\partial^2 F_t}{\partial V_G^2}\right)_{n_G} = -\frac{\mathrm{d}p_G}{\mathrm{d}V_G} + \gamma_{LG}\frac{\mathrm{d}\kappa}{\mathrm{d}V_G} = \frac{p_G}{V_G} + \gamma_{LG}\frac{\mathrm{d}\kappa}{\mathrm{d}V_G} > 0. \tag{2.3}$$

This criterion indicates that the rate of curvature change ($\mathrm{d}\kappa/\mathrm{d}V_G$), which is determined by the surface structure, has a significant impact on the mechanical stability of the gas bubble. Specifically, if the rate of curvature change is positive ($\mathrm{d}\kappa/\mathrm{d}V_G > 0$), then the mechanical equilibrium state is always stable. Moreover, an alternative criterion to determine the stability can be given out by examining the change of equilibrated volume at different ambient liquid pressures. Combining Laplace equation $p_G - p_L = \gamma_{LG}\kappa$ and (2.3), we can obtain a new criterion for the mechanically stable equilibrium state:

$$\frac{\mathrm{d}V_G}{\mathrm{d}p_L} = \left(\frac{\mathrm{d}p_G}{\mathrm{d}V_G} - \gamma_{LG}\frac{\mathrm{d}\kappa}{\mathrm{d}V_G}\right)^{-1} = -\left(\frac{\partial^2 F_t}{\partial V_G^2}\right)_{n_G}^{-1} < 0. \tag{2.4}$$

That is, when increasing the liquid pressure, the volume of the gas bubble that is in mechanical equilibrium should shrink for the stability requirement.

Once the gas bubble reaches a stable mechanical equilibrium (notice that a static gas bubble that can be observed in the experiment is always mechanically stable), the gas diffusion dominates the bubble evolution. During this process, since the gas bubble is in mechanical equilibrium, one can determine the gas mole number n_G by combining Laplace equation $p_G - p_L = \gamma_{LG}\kappa$ with the ideal gas law ($p_G V_G = n_G RT$). By simplifying (2.2), the first-order derivative of free energy with respect to the gas mole number n_G is written as $\mathrm{d}F_t/\mathrm{d}n_G = RT\ln[p_G/(s p_L)]$. Then the second-order derivative of free energy reads $\mathrm{d}^2 F_t/\mathrm{d}n_G^2 = RT\,\mathrm{d}p_G/(p_G\,\mathrm{d}n_G) = \gamma_{LG}\,RT\,\mathrm{d}\kappa/(p_G \mathrm{d}n_G)$.

https://doi.org/10.1017/jfm.2025.10760 Published online by Cambridge University Press

Caption	r	r_B	r_C	r_X	h_C	Θ	s	H
Figure 1(c)	10 nm						143.77	10 cm
Figure 1(e)		50 nm				157.4°	12.00	10 cm
Figure 1(g)		50 nm				157.4°	12.00	10 cm
Figure 1(i)		50 nm				22.6°	12.00	10 cm
Figure 1(k)		50 nm				22.6°	12.00	10 cm
Figure 1(m)			50 μm		100 μm	105.0°	0.99	10 cm
Figure 1(o)			50 μm		100 μm	105.0°	0.99	10 cm
Figure 1(q)		50 μm	150 μm		300 μm	157.4°	0.99	10 cm
Figure 1(s)		50 μm	150 μm		300 μm	157.4°	0.99	10 cm
Figure 1(u)				10.6 μm		120.0°	1.07	10 cm
Figure 1(w)				13.5 μm		120.0°	0.92	10 cm

Table 1. Specific parameters used for calculating the free energy curves shown in figure 1.

Therefore, a diffusion stable gas bubble that can sustain for a long time requires

$$\frac{\mathrm{d}\kappa}{\mathrm{d}n_G} > 0. \tag{2.5}$$

Equation (2.5) is the necessary and sufficient condition for the stable state of underwater gas bubbles, which is independent of bubble-attached conditions, bubble size, wettability and morphology of the attached solid surface. Therefore, it is a universal criterion for evaluating underwater bubble stability. Equation (2.5) describes a competitive balance between gas diffusion and Laplace pressure, i.e. when gas dissolves from the bubble into the surrounding liquid, the morphological change of a stable bubble should result in an increasing curvature such that the reduced gas pressure in the bubble (due to increased Laplace pressure) will lead to gas diffusion from the surrounding liquid back into the bubble. The gas molecules diffusing between the bubbles and the surrounding water reach a balance, making the gas layer keep a stable state.

2.2. *Verification of the criterion for underwater bubbles stability under various conditions*

The stability of bubbles under various conditions is analysed using the criterion in (2.5). The results for suspended bubbles are shown in figure 1(b). When the gas mole number inside the bubble increases ($\mathrm{d}n_G > 0$), the curvature of bubbles with different radii always decreases ($\mathrm{d}\kappa < 0$), resulting in $\mathrm{d}\kappa/\mathrm{d}n_G < 0$. This finding demonstrates that suspended bubbles cannot achieve a stable state, regardless of bubble size, surrounding pressure or dissolved gas saturation. To validate this prediction, the free energy of suspended bubbles is analysed (figure 1c). Under oversaturated water conditions ($s = 143.77$), an equilibrium state can be found ($\delta F_t = 0$) at $r = 10$ nm. Details of the conditions are provided in table 1. However, the energy curve at this equilibrium point (as the dashed line shows) is convex, demonstrating unstable conditions. Therefore, the conclusion of the free energy analysis aligns with the prediction of the criterion. The conclusion that suspended bubbles are unstable is consistent with findings reported in other literature, further supporting the criterion (Plesset & Sadhal 1982; Lohse & Zhang 2015*b*; Tan *et al.* 2021).

The results for bubbles attaching to a flat surface are shown in figure 1(d–k). It is found that the stability criterion (2.5) is satisfied only on a hydrophobic surface with contact line pinning (figure 1d). In this specific condition, bubbles can be stable. In contrast, for hydrophobic surfaces without pinning (figure 1f), hydrophilic surfaces with pinning

https://doi.org/10.1017/jfm.2025.10760 Published online by Cambridge University Press

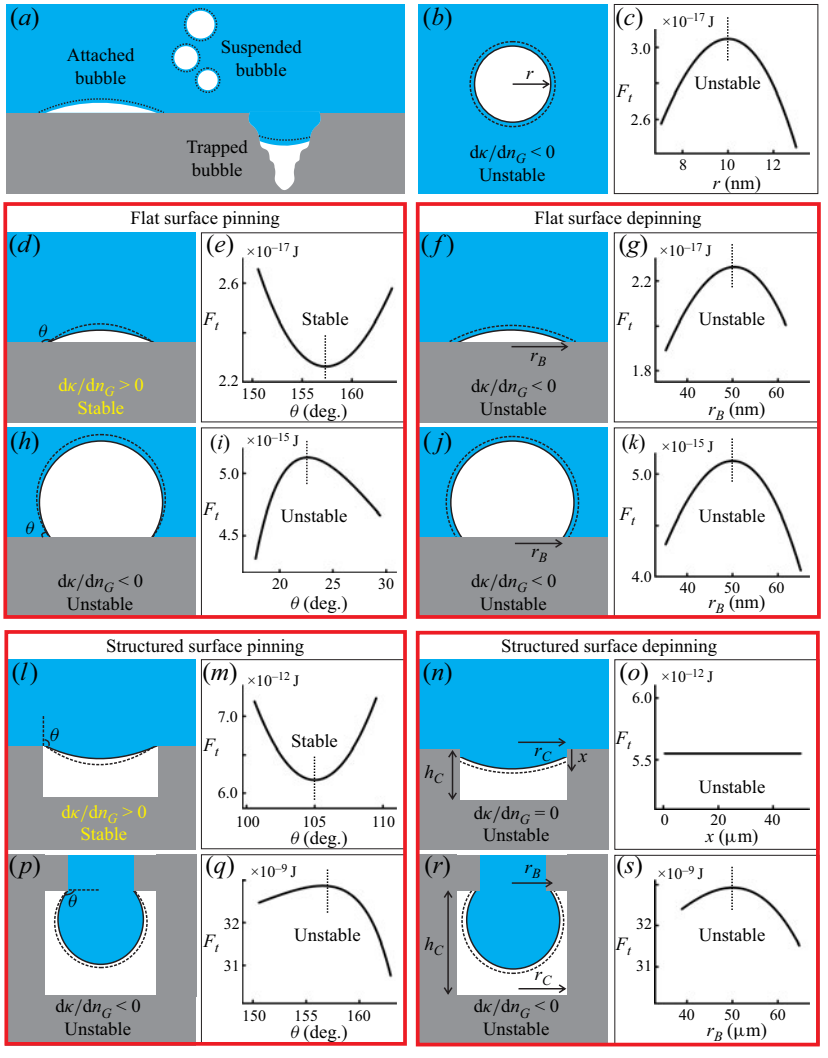


Figure 1. For caption see next page.

(figure 1*h*), or hydrophilic surfaces without pinning (figure 1*j*), bubbles do not achieve a stable state. (The specific case of gas molecule adsorption at the solid–liquid interface is not considered in this discussion; see Brenner & Lohse (2008).) These predictions are further validated by free energy analyses of nanobubbles, as shown in figures 1(*e*), 1(*g*), 1(*i*) and 1(*k*). The analyses confirm that stable states exist only for the pinned hydrophobic surfaces, consistent with the predictions of the criterion. This conclusion is also supported by other literature (Lohse & Zhang 2015*b*; Tan *et al.* 2021; Zhang *et al.* 2024), such as the Lohse–Zhang model (Lohse & Zhang 2015*b*).

The stability analysis of bubbles that are trapped in the surface structures is presented in figure 1(*l–s*). Similar to bubbles attached to flat surfaces, a stable state is found only on a hydrophobic surface with contact line pinning (figure 1*l*) (Xu *et al.* 2014; Xiang *et al.* 2017). For hydrophilic surfaces with contact line pinning, bubbles do not achieve a stable state (figure 1*p*). These predictions are validated through free energy analysis (figure 1*m*,*q*) using micrometre-sized bubbles. The other two conditions, i.e. hydrophobic surfaces

https://doi.org/10.1017/jfm.2025.10760 Published online by Cambridge University Press

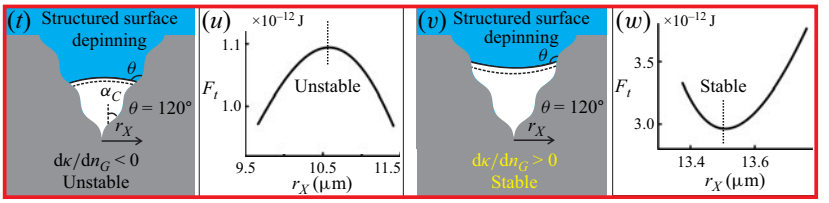


Figure 1. (cntd). Underwater bubble stability under different conditions. (*a*) Schematics of underwater gas bubbles, including suspended, attached and trapped bubbles. Here, bubble broadly refers to underwater gas bubbles and gas layers of various morphologies. (*b*) Schematic diagram of suspended bubbles. Since $\mathrm{d}\kappa/\mathrm{d}n_G < 0$, the criterion is not met, indicating that the bubble is unstable. (*c*) Free energy diagram of suspended bubbles ($r \sim 10$ nm); as the free energy curve is convex, the equilibrium point is unstable. The red lines mark the equilibrium points. (*d–k*) Stability analysis of bubbles attached to flat surfaces. All the bubbles in the energy diagrams are on the nanometre scale, and r_B is approximately 50 nm. (*d*) On a hydrophobic surface with contact line pinning, $\mathrm{d}\kappa/\mathrm{d}n_G > 0$, indicating a stable state. (*e*) Free energy diagram of (*d*), showing a stable state at the equilibrium point. In conditions of (*f*) hydrophobic surfaces without pinning, (*h*) hydrophilic surfaces with pinning, and (*j*) hydrophilic surfaces without pinning, all $\mathrm{d}\kappa/\mathrm{d}n_G < 0$, indicating unstable bubbles. (*g*), (*i*) and (*k*) are the energy diagrams corresponding to (*f*), (*h*) and (*j*), respectively, confirming that all bubbles are unstable. (*l–s*) Stability analysis of bubbles trapped in structured surfaces. All bubbles in the energy diagrams are at the micrometre scale, $r_C = 50\,\mu$m. (*l*) On a hydrophobic surface with contact line pinning, $\mathrm{d}\kappa/\mathrm{d}n_G > 0$, indicating a stable state. (*m*) Free energy diagram of (*l*), showing the stable state at the equilibrium point. (*n*) Bubbles on hydrophobic surfaces without pinning, $\mathrm{d}\kappa/\mathrm{d}n_G = 0$, indicating mechanical equilibrium but not diffusion equilibrium. (*o*) Energy diagram of (*n*). The free energy profile along the horizontal axis indicates that the system is in a special unstable state. (*p*,*q*) Water enters a hydrophilic cavity with pinning, showing no stable state. (*r*,*s*) Water enters a hydrophilic cavity without pinning, showing no stable state. A cavity with sinusoidal walls (*t*,*u*) has no stable state at $r_X = 10.6\,\mu$m, but (*v*,*w*) exhibits a stable state at $r_X = 13.5\,\mu$m.

(figure 1*n*) and hydrophilic surfaces (figure 1*r*) without contact line pinning, also show that no stable state exists. The condition in figure 1(*n*) requires special attention, as the curvature of the liquid–gas interface remains constant regardless of variations in the number of gas molecules within the bubble, i.e. $\mathrm{d}\kappa/\mathrm{d}n_G = 0$. Consequently, gas molecules will continuously dissolve out of or into the bubble, indicating that the system is in a unstable state, which satisfies mechanical equilibrium but does not achieve diffusion equilibrium. This prediction can be verified by the free energy graphs, which show a straight line along the horizontal axis (figure 1*o*). Such states have also been observed experimentally, and have been discussed in previous studies (Poetes *et al.* 2010; Lv *et al.* 2014).

From the above analysis, it can be concluded that this criterion applies to suspended, attached and trapped bubbles, covering a range of sizes including nanoscale, and extending to both hydrophilic and hydrophobic solid surfaces, including flat and structured geometries. As shown in figure 1, stable bubbles require the contact line to remain pinned, whether on flat (figure 1*d*) or structured (figure 1*l*) surfaces. Furthermore, all experimental observations of stable bubble states reported to date have occurred under contact line pinning conditions (Lohse & Zhang 2015*b*; Prakash, Xi & Patel 2016; Li *et al.* 2017; Xiang *et al.* 2017; Zhang *et al.* 2024). If the contact line depins, then the bubble ultimately dissipates (Koishi *et al.* 2009; Papadopoulos *et al.* 2013; Domingues *et al.* 2018; Tan *et al.* 2021). Then we will explore the stable state that occurs after the contact line depins from the sharp edge.

3. New stable mode for underwater bubbles predicted by the criterion

We investigate the stability of bubbles under conditions where the contact line is not pinned on the sharp edge. Bubble motion generally occurs in two distinct modes: (i) the pinning mode, in which the contact line remains fixed while the contact angle

https://doi.org/10.1017/jfm.2025.10760 Published online by Cambridge University Press

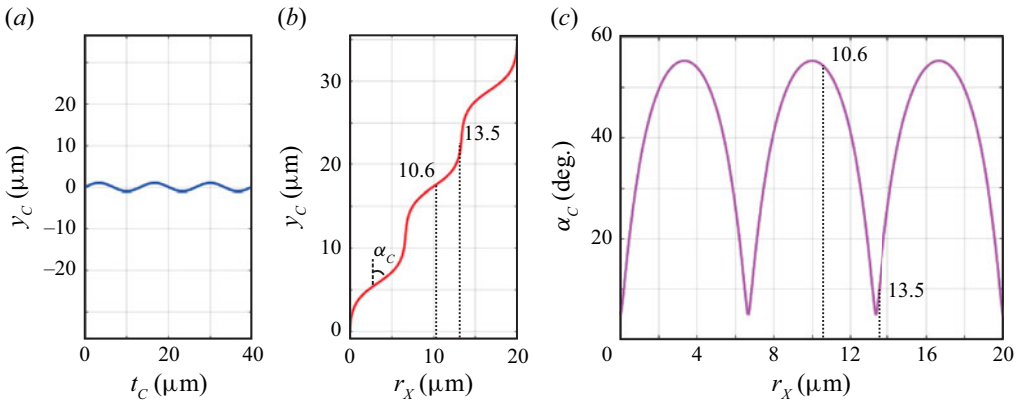


Figure 2. Design of the cavity with walls shaped as a solid of revolution of the sine function. (*a*) Original sine function: $y_C = \sin(3\pi t_C/20)$, with t_C ranging from 0 to 40 μm. (*b*) Rotation of the original sine function by 60° anticlockwise around the origin (0, 0), given by the transformation equations $r_X = \cos(-60°)\, t_C + \sin(-60°)\sin(3\pi t_C/20)$, $y_C = -\sin(-60°)\, t_C + \cos(-60°)\sin(3\pi t_C/20)$, with t_C ranging from 0 to 40 μm. (*c*) The relationship between the rotated curve's half corner angle α_C versus r_X. The vertical dotted lines mark $r_X = 10.6$ μm and $r_X = 13.5$ μm, respectively.

can vary, and (ii) the depinning mode, in which the contact line can move while the contact angle remains constant. Traditionally, stable underwater bubbles on structured surfaces have been attributed to the pinning mode. However, through theoretical analysis, we demonstrate a new type of stable state that arises after depinning from the top sharp edges. Therefore, a geometric standard for solid surfaces supporting the new stable state is proposed and proved by experiments. Using this criterion, we develop a method to control bubble stability by optimising surface geometry.

3.1. *Theoretical analysis of the new stable mode*

We examine the stability of the bubble in a cavity with walls shaped as a solid of revolution of the sine function, $y_C = \sin(3\pi t_C/20)$ (figures 1(*t*) and 2). The contact line is free to move along the cavity walls while maintaining constant contact angle 120°. Because the sidewall is curved, the liquid–gas interface adopts different curvatures in distinct regions: a convex curvature ($\kappa > 0$) when $\alpha_C > 33°$ (figure 1*t*) and a concave curvature ($\kappa < 0$) when $\alpha_C < 33°$ (figure 1*v*). Focusing on the convex region at $r_X = 10.6$ μm (figure 1*t*), an increase in the gas mole number ($\mathrm{d}n_G > 0$) leads to an increased r_X and a decrease in α_C (figure 2). The changes in both r_X and α_C induce a reduction in curvature κ. That yields $\mathrm{d}n_G/\mathrm{d}\kappa < 0$, indicating the unstable state. This conclusion is further supported by the free energy analysis (figure 1*u*). This finding aligns with previous understanding that a stable state requires contact line pinning.

In contrast, in the concave region at $r_X = 13.5$ μm (figure 1*v*), an increase in the gas mole number ($\mathrm{d}n_G > 0$) results in increases in both r_X and α_C (figure 2), which leads to $\mathrm{d}\kappa > 0$, and yields $\mathrm{d}n_G/\mathrm{d}\kappa > 0$. This indicates a stable state even as the contact line depins and moves, as confirmed by free energy analysis in figure 1, which demonstrates a new stable mode of surface bubble that has not been reported before. Moreover, our results show that bubble stability depends on surface geometry, with certain regions on a curved wall supporting a stable state, while others do not.

https://doi.org/10.1017/jfm.2025.10760 Published online by Cambridge University Press

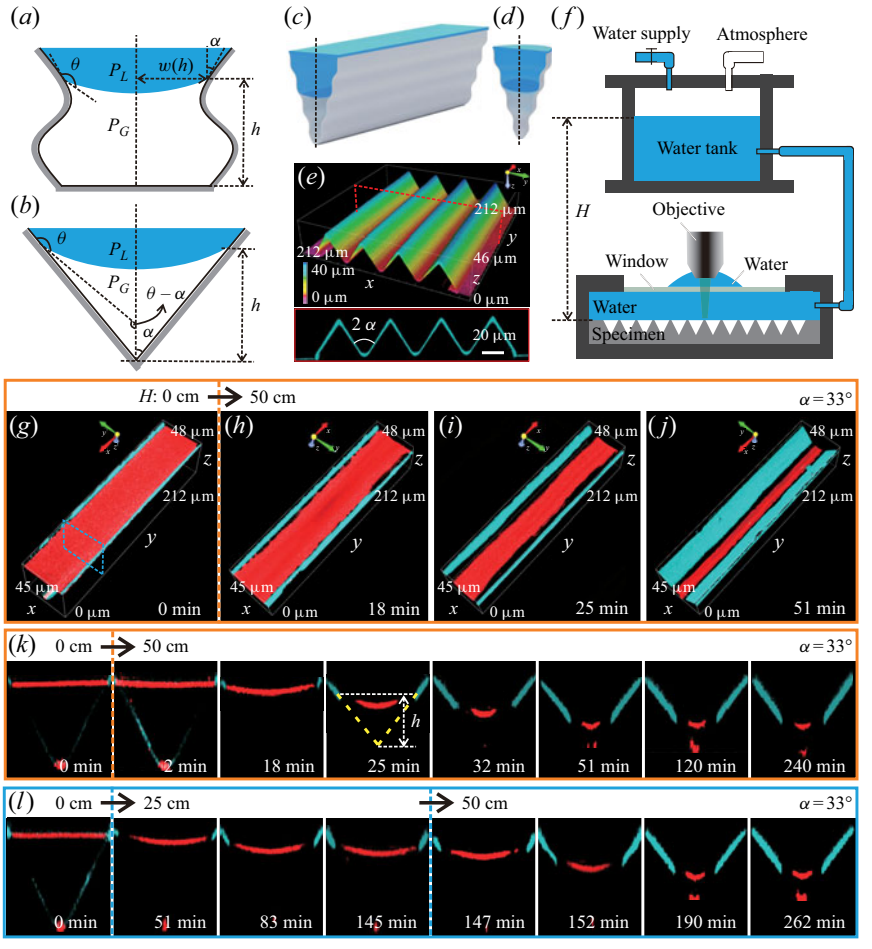


Figure 3. For caption see next page.

3.2. *Geometric standard for solid surfaces supporting the new stable mode*

Next, we will explore the specific surface geometries required for the bubble stable state. Equation (2.5) is applied to cavities with smooth sidewalls, ensuring the absence of contact line pinning. For simplicity, but without loss of generality, we select widely accepted topological models to represent cavity geometries: two-dimensional (2-D) grooves (a groove with uniform cross-section, figure 3*a*,*b*) with an arbitrary but symmetric profile (figure 3*c*) and three-dimensional (3-D) rotational symmetric pores (figure 3*d*). The generatrix of the groove or the pore is characterised by $w(h)$. The mechanical stability is hard to discuss analytically as it involves integrating the profile when calculating the gas volume. But in an experiment, as long as we can observe a non-dynamic gas bubble, it must be a mechanical stable equilibrium. For simplicity, we assume that the gas bubble is already mechanically stable. Under this assumption, the equilibrium position of gas dissolution satisfies $\gamma_{LG}\cos(\theta_Y-\alpha(h))/w(h)=p_L(s-1)$. The stability criteria (2.5) for gas diffusion can be simplified as

$$\frac{\mathrm{d}\kappa}{\mathrm{d}n_G}=\frac{\mathrm{d}\kappa}{\mathrm{d}h}\frac{\mathrm{d}h}{\mathrm{d}n_G}=\frac{w\,(h)\,\alpha'\,(h)\sin\left(\theta_Y-\alpha\,(h)\right)-w'\,(h)\cos\left(\theta_Y-\alpha\,(h)\right)}{w\,(h)^2}\frac{\mathrm{d}h}{\mathrm{d}n_G}>0. \tag{3.1}$$

https://doi.org/10.1017/jfm.2025.10760 Published online by Cambridge University Press

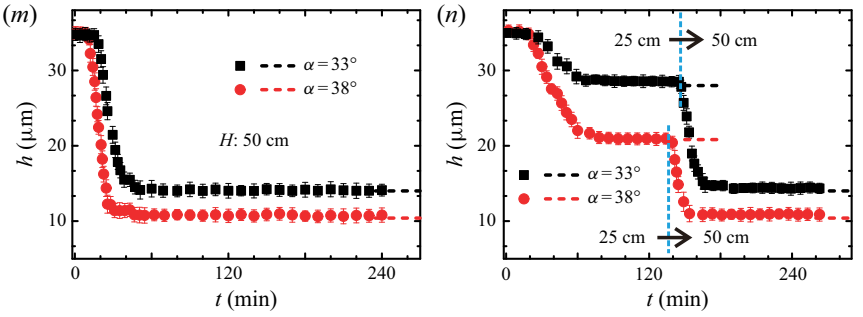


Figure 3. (cntd). Stable state of gas bubbles without contact line pinning. Schematics of symmetric cross-sections with (*a*) arbitrary and (*b*) wedge profiles, where $w(h) = \tan(\alpha)\, h$, and α is a constant; (*c*) 2-D grooves with arbitrary profile, and (*d*) 3-D rotational symmetric pores. (*e*) Confocal images of the wedge-groove specimens with half corner angle $\alpha = 33 \pm 1.7°$, for top, 3-D images, and bottom, 2-D profile. (*f*) Experimental set-up: a sample fixed in a sealed resin glass box connected to a water tank. The submerged depth H is adjusted by changing the vertical position of the water tank. Deionised water, saturated with atmospheric pressure over 2 days, is used. The evolution of the air layer is observed through a 40× water immersion objective via an optical glass window. (*g–j*) The 3-D confocal images showing liquid–gas interface evolution as H increases from 0 to 50 cm. Cyan indicates wedge groove wall; red indicates liquid–gas interface. (*k*) Cross-section images of the liquid–gas interface from (*g*), with H increasing from 0 to 50 cm, where h is the vertical distance from contact lines to the wedge groove tip. Due to light scattering near the curved liquid surface, the liquid–gas interface close to the wall is not clearly visible. To address this, a quadratic curve fitting method is applied to the interface contour to estimate the local profile and calculate the contact angle between the interface and the wall. (*l*) Cross-section images with H increasing from 0 to 25 cm, then from 25 to 50 cm. (*m,n*) Quantified h evolution from (*k*) and (*l*), with experimental results indicated by black squares ($\alpha = 33°$) and red dots ($\alpha = 38°$); see supplementary material figure S3 for details available at https://doi.org/10.1017/jfm.2025.10760. Dashed lines indicate theoretical prediction of h using (3.8).

where $\alpha'(h) = w''(h)\cos^2\alpha$. In order to calculate the sign of $\mathrm{d}h/\mathrm{d}n_G$, we apply derivative regarding h to the ideal gas law and combine it with Laplace equation $p_G - p_L = \gamma_{LG}\kappa$ and (2.3),

$$RT\frac{\mathrm{d}n_G}{\mathrm{d}h} = \left(\gamma_{LG}\frac{\mathrm{d}\kappa}{\mathrm{d}V_G} + \frac{p_L + \gamma_{LG}\kappa}{V_G}\right)\frac{\mathrm{d}V_G}{\mathrm{d}h}V_G = \left(\frac{\partial^2 F_t}{\partial V_G^2}\right)_{n_G}\frac{\mathrm{d}V_G}{\mathrm{d}h}V_G. \tag{3.2}$$

Notice that the sign of $(\partial^2 F_t/\partial V_G^2)_{n_G}$ denotes the mechanical stability, where positive and negative signs represent stable and unstable states, respectively. Then for a mechanically stable gas bubble, assuming that V_G is a monotonic increasing function of h ($\mathrm{d}V_G/\mathrm{d}h > 0$), we can find that $\mathrm{d}h/\mathrm{d}n_G > 0$. Therefore, the stability criteria (3.2) for gas diffusion can be simplified as

$$w(h)\,\alpha'(h)\sin(\theta_Y - \alpha(h)) > \tan(\alpha(h))\cos(\theta_Y - \alpha(h)). \tag{3.3}$$

Notice that Young's contact angle is in the range $\theta_Y \in [0, \pi]$. If we assume that $\alpha \in [-\pi/2, \pi/2]$, which indicates that a certain value of h only refers to one position of the interface, then we can simplify the stability criterion as

$$\alpha'(h) > \frac{\tan(\alpha(h))\cot(\theta_Y - \alpha(h))}{w(h)} \quad \text{if } \theta_Y - \alpha(h) \in (0, \pi), \tag{3.4a}$$

$$\alpha'(h) < \frac{\tan(\alpha(h))\cot(\theta_Y - \alpha(h))}{w(h)} \quad \text{if } \theta_Y - \alpha(h) < 0 \text{ or } \theta_Y - \alpha(h) > \pi. \tag{3.4b}$$

Although (3.4) defines the sufficient and necessary condition for the stability criterion, it is too complicated to be applied in practice. With some simplification, we can find two

https://doi.org/10.1017/jfm.2025.10760 Published online by Cambridge University Press

simpler, sufficient but not necessary conditions of the diffusion stable state:

$$\alpha\,(h) > 0,\ \alpha'(h) \geq 0 \quad \text{and} \quad \theta_Y - \alpha\,(h) > \pi/2, \tag{3.5a}$$

$$\text{or} \quad \alpha\,(h) < 0,\ \alpha'(h) \geq 0 \quad \text{and} \quad 0 < \theta_Y - \alpha\,(h) < \pi/2. \tag{3.5b}$$

Equation (3.5*a*) describes a scenario on hydrophobic surfaces, where the cavity must exhibit an increasing width and a non-decreasing inclining angle from the bottom to the top, and the angle $\alpha(h)$ does not exceed the limit $\theta_Y - \pi/2$. Equation (3.5*b*) describes a scenario of hydrophilic cavities, where the width should decrease and the angle should not decrease from the bottom to the top, and the angle $\alpha(h)$should be limited to $[\theta_Y - \pi/2, \theta_Y]$. Specifically, for a wedge groove with constant angle $\alpha > 0$, the meniscus curvature for a gas bubble is written as $\kappa = \cos(\theta_Y - \alpha)/(h\tan\alpha)$. Then the stability criteria can be rigorously found by simplifying (2.5) together with $\mathrm{d}h/\mathrm{d}n_G > 0$, which reads

$$\theta_Y - \alpha\,(h) > \pi/2, \tag{3.6}$$

which coincides with sufficient but not necessary conditions (3.5*a*).

Then the equilibrium position of the contact line will be analysed as follows. In the wedge groove, the curvature of the liquid–gas interface can be expressed as $\kappa = \cos(\theta - \alpha)/(h\tan\alpha)$, where h is the vertical distance from the contact line to the tip of the wedge groove. Substituting κ into the equilibrium equation, i.e. $\gamma_{LG}\cos(\theta_Y - \alpha(h))/w(h) = p_L(s-1)$, we can obtain the equilibrium position of contact lines:

$$h = \frac{\gamma_{LG}\cos(\theta - \alpha)}{\tan\alpha}\frac{1}{p_L\,(s-1)}. \tag{3.7}$$

It can be found from (3.7) that different positions of the liquid–gas interface h correspond to different environmental conditions (p_L, s), indicating that the stable state has the potential to spontaneously adapt to the variations of the environmental conditions by changing its positions. Moreover, in the condition of the experiment in the main text, the gas saturation degree is $s = p_a/p_L$, which renders (3.7) to be simplified as

$$h = \frac{-\gamma_{LG}\cos(\theta - \alpha)}{\rho g\tan\alpha}\frac{1}{H}. \tag{3.8}$$

If the liquid–gas interface remains in this equilibrium position over an extended period, then we can conclude that the bubbles are in a stable state.

Similar to the above analysis on a 2-D symmetric groove, we can also discuss the diffusion stability for a 3-D pore with a rotational symmetric profile. Denote $r = w(h)$ as the radius of the pore, and h as the vertical distance from the point of interest to the bottom of the pore. For a gas bubble at height h, the meniscus curvature can be found by $\kappa = 2\cos(\Theta_Y - \alpha(h))/r$, where $\tan(\alpha) = w'(h)$. Compared to the 2-D groove, the interface curvature of the 3-D pore only has an additional factor 2, which does not have any impact when applying the stability criterion (2.5). Therefore, the above results for the diffusion stability as (3.3)–(3.8) also hold for the rotational symmetric 3-D pore.

3.3. *Experimental evidence for the new stable state and geometric standard*

Experiments are carried out to prove that stable states can be achieved without contact line pinning. The wedge grooves with different corner angles 2α (figure 3(*e*) and supplementary material figure S1) are fabricated with the photoresist SU-8 (MicroChem Corp., USA) using a 3-D laser lithography system (Photonic Professional GT, Nanoscribe GmbH, Germany) (Xiang *et al.* 2020), and then are hydrophobised with a commercial hydrophobic agent (Glaco, Japan) to achieve contact angle $\theta = 156 \pm 5.2°$. A laser

https://doi.org/10.1017/jfm.2025.10760 Published online by Cambridge University Press

scanning confocal microscope (A1R-PLUS, Nikon, Japan) is employed to observe the evolution of the liquid–gas interface in wedge grooves. The liquid pressure on the wedge grooves (p_L) is composed of the atmospheric pressure (p_a) and the hydrostatic pressure ($\rho g H$), i.e. $p_L = p_a + \rho g H$, where ρ is the water density, g is gravity, and H is the submerged depth of the wedge grooves (figure 3*f*).

Experimental images illustrating the submerged depth H changing from 0 to 50 cm are as shown in figure 3(*g–k*), while the evolution of the meniscus position h is presented in figure 3(*m*). Over time, the liquid–gas interfaces depin from the top edge of the wedge and freely move in the wedge. After 51 min of evolution (figure 3*k*), their positions remained unchanged. From the perspective of gas and mass transport dynamics, the diffusion time scale is approximately 100 s (Lv *et al.* 2014). Therefore, the 51 min observation period is sufficient for the bubble to reach a stable state. Moreover, by comparing the final value of h with the theoretical prediction of (3.8) in figure 3(*m*), it is confirmed that the liquid–gas interface reaches a stable state. Subsequently, experiments are conducted with H changing twice, and the results are shown in figures 3(*l*) and 3(*n*). First, when H changes from 0 to 25 cm, the liquid–gas interface reaches a stable state for the first time (from 83 min to 145 min). Then as H changes from 25 to 50 cm, the liquid–gas interface reaches a new stable state (from 190 min to 262 min). These experiments demonstrate the existence of a stable state without contact line pinning, and show that the freely moving contact line allows the system to adapt to changing environmental conditions.

The geometric standard for solid surfaces supporting the stable state is experimentally verified. Figures 4(*a*) and 4(*b*) show a stable gas column that remains unchanged for over 240 min when (3.5*a*) is satisfied. In contrast, figures 4(*c*) and 4(*d*) show that when (3.5*a*) is not satisfied, the gas column breaks into shrinking segments and disappears within 9 min. The cause of this segmentation is detailed in Concus & Finn (1969, 1974), Langbein (1990) and Xiang *et al.* (2020). The phase diagram for the stable state is shown in figure 4(*e*), with the threshold line defined by $\alpha = \theta - \pi/2$. The region to the right of the curve, where (3.5*a*) is satisfied, represents the stable state, while the left-hand region, where (3.5*a*) is not satisfied, corresponds to the regime where bubbles gradually shrink and eventually disappear. To validate the phase diagram, experiments test the stability of gas bubbles in grooves with varying corner angles 2α and contact angles θ. Solid points and hollow points in figure 4(*e*) represent the stable state and the fully wetted state, respectively. The experimental results align with the theoretical prediction of the phase diagram (additional results are available in supplementary material figure S3). Energy diagrams in figures 4(*f*) and 4(*g*) further confirm this. Figure 4(*f*) matches the energy profile of a fully wetted state, and figure 4(*g*) matches the stable gas state. These energy diagrams confirm, from a thermodynamic perspective, that gas bubbles can remain in a stable state when the solid surface adheres to the proposed geometric standard.

The critical conditions for achieving a stable state are analysed based on (3.8), which shows that the submerged depth H is inversely proportional to the interface position h. Since the tip point of the groove cannot form a geometric singularity, h has a minimum value h_{min} (figure 4*h*). Correspondingly, H has the maximum value $H_{max} = -\gamma L_G \cos(\theta - \alpha)/\rho g \tan(\alpha)\, h_{min}$. Then the limitation H_{max} is experimentally verified. The lines in figure 4(*i*) correspond to the theoretical predictions from (3.8). The intersections of the solid and dashed lines denote the theoretical critical points (H_{max}, h_{min}). The solid parts of the lines represent conditions within the critical boundary ($H < H_{max}$) where a stable state is maintained, while the dashed parts ($H > H_{max}$) indicate an unstable state. Experimental data, shown as solid and open dots, represent stable (lasting over 2 h) and unstable (vanishing within 30 min) liquid–gas interfaces, respectively. The experimental results (dots) are consistent with the theoretical predictions

https://doi.org/10.1017/jfm.2025.10760 Published online by Cambridge University Press

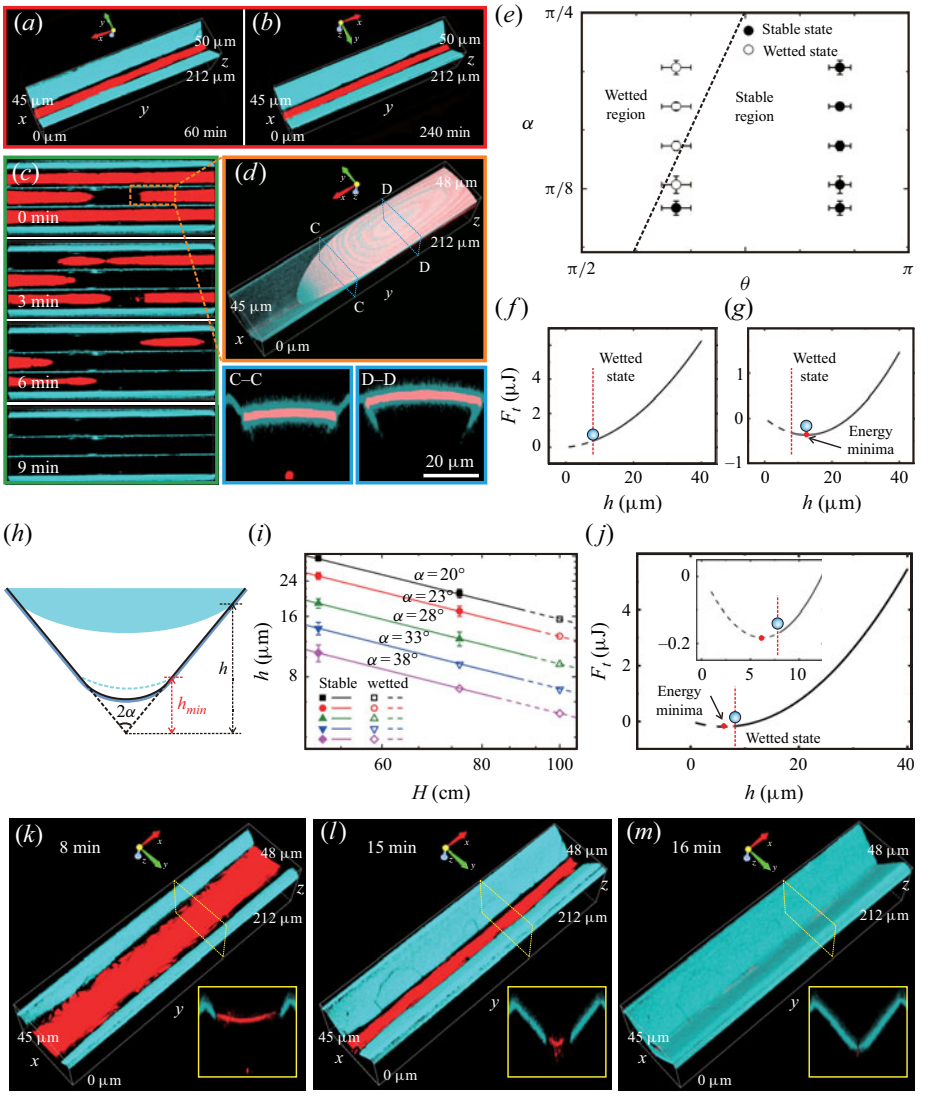


Figure 4. Geometry standard of solid surface supporting stable state. (*a*,*b*) Confocal images of stable gas bubbles, where $\theta = 156°$, $\alpha = 33°$ and $H = 50$ cm. (*c*) Gas bubbles evolution in the wedge groove, where $\theta = 116°$, $\alpha = 33°$ and $H = 50$ cm. (*d*) Enlarged image of (*c*). The insets of C–C and D–D show the cross-sections of the dotted boxes of the 3-D image. The menisci are convex. (*e*) Phase diagram of the stable states of gas bubbles, where the right- and left-hand regions indicate the stable state and fully wetted state, respectively. Energy diagrams of (*f*) the fully wetted state with $\theta = 116°$, $\alpha = 33°$ and $H = 50$ cm, and (*g*) the stable state with $\theta = 156°$, $\alpha = 33°$ and $H = 50$ cm. The red dot represents the energy local minima of the free energy curve. The blue ball indicates the minimum energy state that can be achieved in practice. (*h*) Schematics of the liquid–gas interface in the wedge groove corner. (*i*) Dependence of the contact line position h on submerged depth H. Lines show the theoretical prediction of (3.8), where the solid parts indicate the cases within the critical boundary, i.e. the stable region, and the dashed parts indicate the cases beyond the critical boundary, i.e. the unstable region. Solid and open dots indicate the experimental results of the stable state and fully wetted state, respectively. (*j*) Energy diagram of the fully wetted state with the wedge groove ($\theta = 116°$, $\alpha = 33°$) satisfies (3.5). Here, the submerged depth $H = 100$ cm exceeds the critical value $H_{max} = 88$ cm. (*k–m*) Images of the liquid–gas interface evolution for (*j*).

https://doi.org/10.1017/jfm.2025.10760 Published online by Cambridge University Press

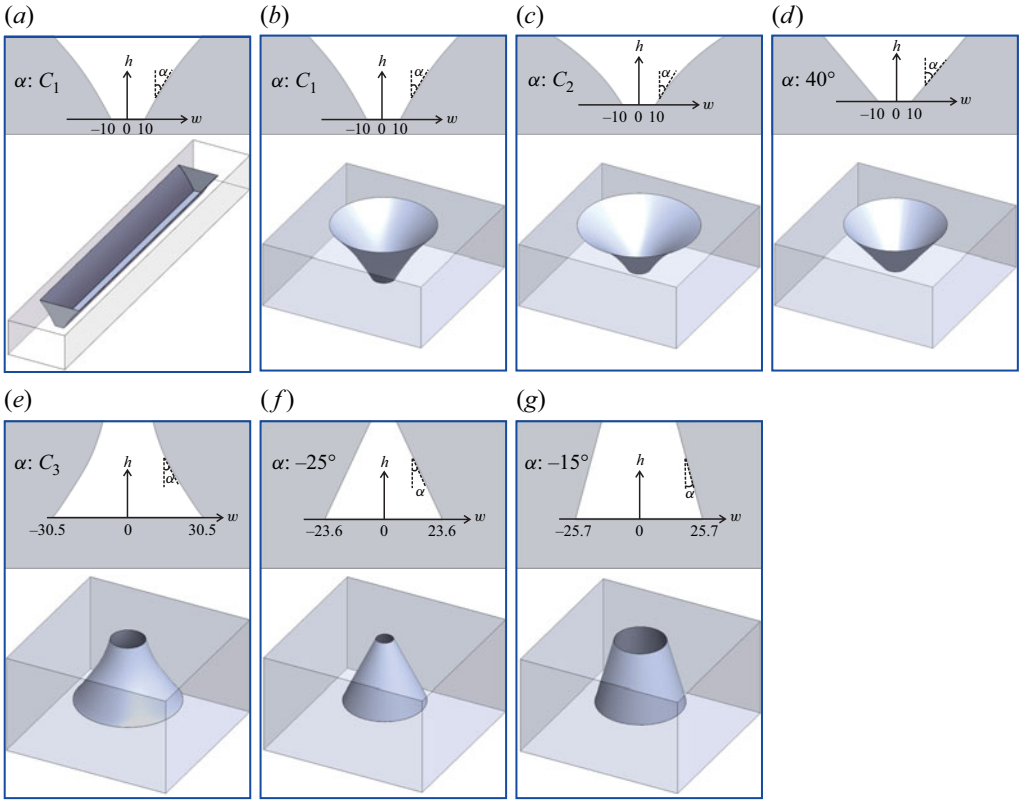


Figure 5. Cross-section profiles and 3-D design drawing images of grooves and pores. For the hydrophobic sample with $\theta = 156°$, the cross-section profiles are (*a*) C_1, $\alpha = 0.009375h^2 + 27$, (*b*) C_1, $\alpha = 0.009375h^2 + 27$, (*c*) C_2, $\alpha = 0.75h + 30$, (*d*) $\alpha = 40°$. For the hydrophilic sample with $\theta = 54°$, the cross-section profiles are (*e*) C_3, $\alpha = -0.015625h^2 + 35$, (*f*) $\alpha = -25°$, (*g*) $\alpha = -15°$. The unit of h here is microns.

(lines) in figure 4(*i*), confirming that H_{max} represents the critical limit of the stable state. Figure 4(*j*) shows the energy diagram for $H > H_{max}$, confirming thermodynamically that no stable state exists. The evolution of gas bubbles under these conditions is shown in figure 4(*k–m*) (with additional data in supplementary material figures S4 and S5). These bubbles transition into a fully wetted state. In addition to grooves, stable gas bubbles can also form in pores, with a similar geometric criterion described by (3.5). Experimental validation for pores is provided in supplementary material figure S6.

3.4. *Controlling gas bubble stability via surface geometry design*

We propose a method to control the stability of gas bubbles under varying environmental conditions by designing the geometry of solid surfaces. There are grooves or pores with generatrix $w(h)$. For submerged depths H_1 and H_2, the stable liquid–gas interface points are $w(h_1)$ and $w(h_2)$, respectively. Detailed information is provided in figure 5. If all points on the piece of the sidewall between $w(h_1)$ and $w(h_2)$ satisfy the geometric standard, then the stable state can be achieved over the depth range from H_1 and H_2. To validate this design method, experiments are conducted on hydrophobic and hydrophilic surfaces under oversaturated and unsaturated water conditions, using both straight and curved generatrix designs. The experimental results for the hydrophobic groove are shown in figure 6(*a–e*). The cross-section profile of the groove C_1 satisfies the criterion (3.5*a*).

https://doi.org/10.1017/jfm.2025.10760 Published online by Cambridge University Press

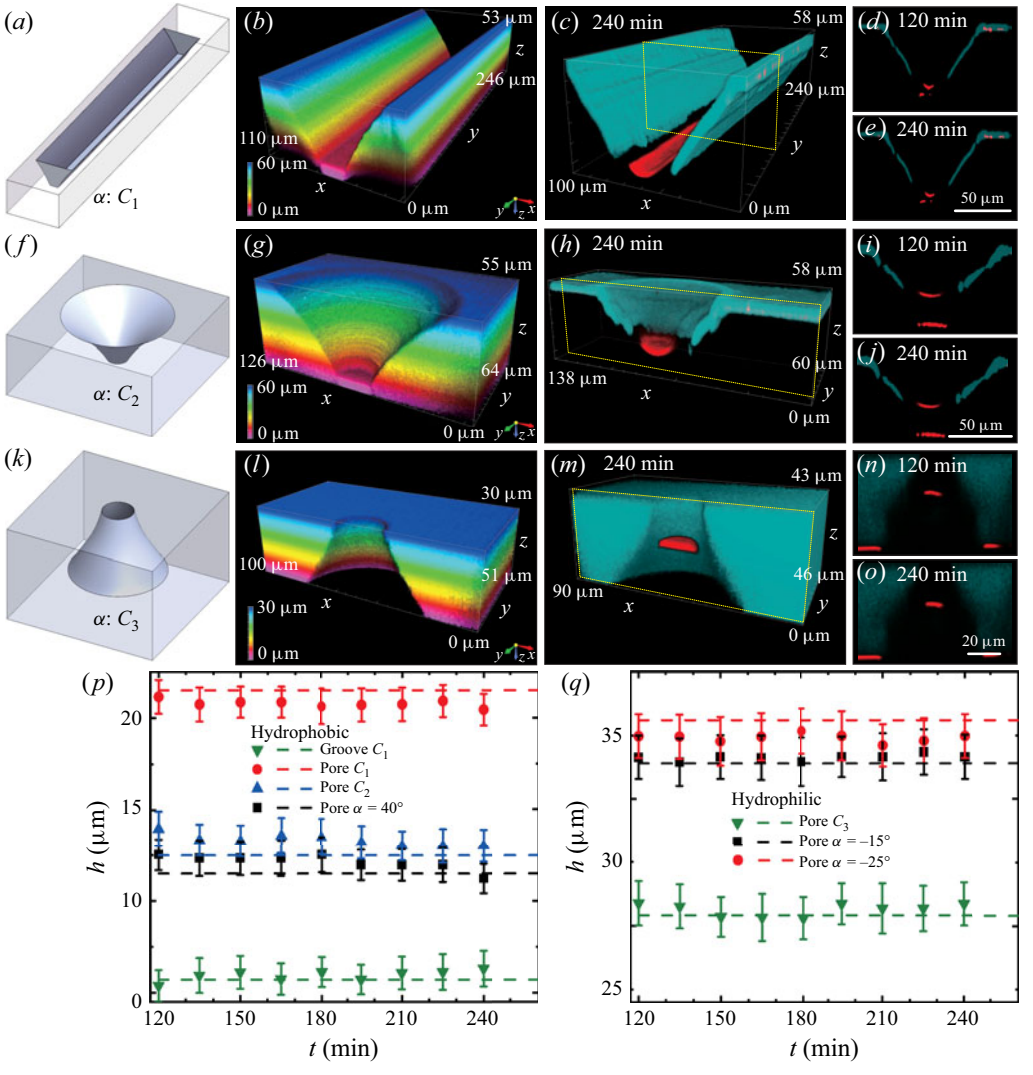


Figure 6. Control the stability of gas bubbles by designing the geometry of solid surfaces. Various structured solid surfaces are designed to stabilise the gas bubble. (*a*,*b*) A 3-D design drawing and confocal image of groove with the generatrix C_1, $\alpha = 0.009375h^2 + 27$. (*c*) Experimental result with $\theta = 156°$ and $H = 30$ cm. (*d*,*e*) Cross-section images with submersion times 120 min and 240 min, respectively. (*f*,*g*) Design drawing and confocal image of pore with the generatrix C_2, $\alpha = 0.75h + 30$. (*h–j*) Experimental result with $\theta = 156°$ and $H = 30$ cm. (*k*,*l*) Design drawing and confocal image of pore with the generatrix C_3, $\alpha = -0.015625h^2 + 35$. (*m–o*) Experimental result with $\theta = 54°$ and $H = -30$ cm. (*p*) Evolution of the liquid–gas interface in hydrophobic grooves and pores after submersion for over 120 min. For all samples, $\theta = 156°$ and $H = 30$ cm. (*q*) Experimental results on hydrophilic grooves and pores. For all samples, $\theta = 54°$ and $H = -30$ cm.

Results for hydrophobic and hydrophilic pores are shown in figures 6(*f–j*) and 6(*k–o*). The generatrices C_2 and C_3 satisfy (3.5*a*) and (3.5*b*), respectively. Images in figures 6(*d*), 6(*e*), 6(*i*), 6(*j*), 6(*n*) and 6(*o*) represent the results of these three samples submerged underwater from 120 min to 240 min. These images show that liquid–gas interfaces remain stable over 120 min. Comparing the contact line location with the theoretically predicted stable value, we find that they are in a stable state. More results are shown in figure 6(*p*,*q*),

https://doi.org/10.1017/jfm.2025.10760 Published online by Cambridge University Press

which indicate that these cavities satisfying the geometric standard could make the gas bubbles achieve a stable state (see supplementary material figure S6 for more data).

4. Conclusion

This work proposes a unified framework for analysing the stability of underwater bubbles under different conditions, and proposes a universal stable state criterion. Based on this criterion, a new stable mode of underwater bubbles is demonstrated. Unlike the classical mode, which relies on the contact line pinning effect, in the new mode, the synergetic effect provided by the geometry and wettability of the sidewalls sustains the bubble stable state. The geometry of cavities is found to be responsible for the stability of gas bubbles. Then the geometrical criterion of cavities to make gas bubbles stable is put forward. Following the criterion, a control method of the stability of gas bubbles in given environmental conditions is raised. The finding provides guidance for the optimisation of crevice geometries to control the stability of gas bubbles underwater, which could be used for the regulation of cavitation, boiling, and various chemical reactions.

Supplementary material. Supplementary material is available at https://doi.org/10.1017/jfm.2025.10760.

Acknowledgements. The authors gratefully acknowledge the anonymous reviewers for their constructive comments, which have greatly improved this paper.

Funding. This work is supported by the National Natural Science Foundation of China (NSFC) under grant nos 12293000, 12293001, 11988102, 12172006, U2141251.

Declaration of interests. The authors report no conflict of interest.

References

Adamkowski, A., Henke, A. & Lewandowski, M. 2016 Resonance of torsional vibrations of centrifugal pump shafts due to cavitation erosion of pump impellers. *Engng Fail. Anal.* **70**, 56–72.

Arndt, R.E. 1981 Cavitation in fluid machinery and hydraulic structures. *Annu. Rev. Fluid Mech.* **13**, 273–326.

Atchley, A.A. & Prosperetti, A. 1989 The crevice model of bubble nucleation. *J. Acoust. Soc. Am.* **86**, 1065–1084.

Brenner, M.P. & Lohse, D. 2008 Dynamic equilibrium mechanism for surface nanobubble stabilization. *Phys. Rev. Lett.* **101** (21), 214505.

Chappell, M.A. & Payne, S.J. 2007 The effect of cavity geometry on the nucleation of bubbles from cavities. *J. Acoust. Soc. Am.* **121**, 853–862.

Choi, C.-H. & Kim, C.-J. 2006 Large slip of aqueous liquid flow over a nanoengineered superhydrophobic surface. *Phys. Rev. Lett.* **96** (6), 066001.

Concus, P. & Finn, R. 1969 On the behavior of a capillary surface in a wedge. *Proc. Natl Acad. Sci. USA* **63**, 292–299.

Concus, P. & Finn, R. 1974 On capillary free surfaces in the absence of gravity. *Acta Mathematica* **132**, 177–198.

Domingues, E.M., Arunachalam, S., Nauruzbayeva, J. & Mishra, H. 2018 Biomimetic coating-free surfaces for long-term entrapment of air under wetting liquids. *Nat. Commun.* **9** (1), 3606.

Granick, S., Zhu, Y. & Lee, H. 2003 Slippery questions about complex fluids flowing past solids. *Nat. Mater.* **2** (4), 221–227.

Guichet, V., Almahmoud, S. & Jouhara, H. 2019 Nucleate pool boiling heat transfer in wickless heat pipes (two-phase closed thermosyphons): a critical review of correlations. *Therm. Sci. Engng Prog.* **13**, 100384.

Jones, S.F., Evans, G.M. & Galvin, K.P. 1999 Bubble nucleation from gas cavities – a review. *Adv. Colloid Interface Sci.* **80**, 27–50.

Karimi, A. & Martin, J.L. 1986 Cavitation erosion of materials. *Intl Metal. Rev.* **31**, 1–26.

Koishi, T., Yasuoka, K., Fujikawa, S., Ebisuzaki, T. & Zeng, X.C. 2009 Coexistence and transition between Cassie and Wenzel state on pillared hydrophobic surface. *Proc. Natl Acad. Sci. USA* **106**, 8435–8440.

https://doi.org/10.1017/jfm.2025.10760 Published online by Cambridge University Press

LANGBEIN, D. 1990 The shape and stability of liquid menisci at solid edges. *J. Fluid Mech.* **213**, 251–265.
LI, J., MAYORGA-MARTINEZ, C.C., OHL, C.D. & PUMERA, M. 2022 Ultrasonically propelled micro- and nanorobots. *Adv. Funct. Mater.* **32**, 2102265.
LI, Y., QUÉRÉ, D., LV, C. & ZHENG, Q. 2017 Monostable superrepellent materials. *Proc. Natl Acad. Sci. USA* **114**, 3387–3392.
LIU, G., WONG, W.S., KRAFT, M., AGER, J.W., VOLLMER, D. & XU, R. 2021 Wetting-regulated gas-involving (photo) electrocatalysis: biomimetics in energy conversion. *Chem. Soc. Rev.* **50**, 10674–10699.
LOHSE, D. & ZHANG, X. 2015*a* Pinning and gas oversaturation imply stable single surface nanobubbles. *Phys. Rev. E* **91** (3), 31003.
LOHSE, D. & ZHANG, X. 2015*b* Surface nanobubbles and nanodroplets. *Rev. Mod. Phys.* **87** (3), 981–1035.
LV, P., XUE, Y., SHI, Y., LIN, H. & DUAN, H. 2014 Metastable states and wetting transition of submerged superhydrophobic structures. *Phys. Rev. Lett.* **112**, 196101.
PAPADOPOULOS, P., MAMMEN, L., DENG, X., VOLLMER, D. & BUTT, H.J. 2013 How superhydrophobicity breaks down. *Proc. Natl Acad. Sci. USA* **110**, 3254–3258.
PFEIFFER, P., EISENER, J., REESE, H., LI, M., MA, X., SUN, C. & OHL, C.D. 2022 Thermally assisted heterogeneous cavitation through gas supersaturation. *Phys. Rev. Lett.* **128**, 194501.
PLESSET, M.S. & SADHAL, S.S. 1982 On the stability of gas bubbles in liquid–gas solutions. *Appl. Sci. Res.* **38** (1), 133–141.
POETES, R., HOLTZMANN, K., FRANZE, K. & STEINER, U. 2010 Metastable underwater superhydrophobicity. *Phys. Rev. Lett.* **105** (16), 166104.
PRAKASH, S., XI, E. & PATEL, A.J. 2016 Spontaneous recovery of superhydrophobicity on nanotextured surfaces. *Proc. Natl Acad. Sci. USA* **113**, 5508–5513.
PRENTICE, P., CUSCHIERI, A., DHOLAKIA, K., PRAUSNITZ, M. & CAMPBELL, P. 2005 Membrane disruption by optically controlled microbubble cavitation. *Nat. Phys.* **1**, 107–110.
SRINIVASAN, S., KLEINGARTNER, J.A., GILBERT, J.B., COHEN, R.E., MILNE, A.J.B. & MCKINLEY, G.H. 2015 Sustainable drag reduction in turbulent Taylor–Couette flows by depositing sprayable superhydrophobic surfaces. *Phys. Rev. Lett.* **114** (1), 014501.
SUN, Y., YAO, Z., WANG, C., ZHONG, Q., XIAO, R., OHL, C.-D. & WANG, F. 2025 Dynamics of cavitation bubbles near a gas-entrapping rigid surface. *J. Fluid Mech.* **1013** A9.
TAN, B.H., AN, H. & OHL, C.-D. 2021 Stability of surface and bulk nanobubbles. *Curr. Opin. Colloid Interface Sci.* **53**, 101428.
TEMPRANO-COLETO, F., SMITH, S.M., PEAUDECERF, F.J., LANDEL, J.R., GIBOU, F. & LUZZATTO-FEGIZ, P. 2023 A single parameter can predict surfactant impairment of superhydrophobic drag reduction. *Proc. Natl Acad. Sci. USA* **120** (3), e2211092120.
VERSLUIS, M., SCHMITZ, B., VON DER HEYDT, A. & LOHSE, D. 2000 How snapping shrimp snap: through cavitating bubbles. *Science* **289**, 2114–2117.
WANG, J., ABE, A., KOITA, T., SUN, M., WANG, Y. & HUANG, C. 2018 Study of sterilization effects on marine *Vibrio* sp. using interaction of cavitation with shock wave in a narrow water chamber. *J. Appl. Phys.* **124**, 213301.
XIANG, Y., HUANG, S., HUANG, T.Y., DONG, A., CAO, D., LI, H., 2020 Superrepellency of underwater hierarchical structures on salvinia leaf. *Proc. Natl Acad. Sci. USA* **117**, 2282–2287.
XIANG, Y., HUANG, S., LV, P., XUE, Y., SU, Q. & DUAN, H. 2017 Ultimate stable underwater superhydrophobic state. *Phys. Rev. Lett.* **119**, 134501.
XU, M., SUN, G. & KIM, C.J. 2014 Infinite lifetime of underwater superhydrophobic states. *Phys. Rev. Lett.* **113**, 136103.
XUE, Y., LV, P., LIN, H. & DUAN, H. 2016 Underwater superhydrophobicity: stability, design and regulation, and applications. *Appl. Mech. Rev.* **68**, 030803.
ZHANG, X., CHAN, D.Y.C., WANG, D. & MAEDA, N. 2013 Stability of interfacial nanobubbles. *Langmuir* **29** (4), 1017–1023.
ZHANG, Y. & LOHSE, D. 2023 Minimum current for detachment of electrolytic bubbles. *J. Fluid Mech.* **975**, R3.
ZHANG, Y., ZHU, X., WOOD, J.A. & LOHSE, D. 2024 Threshold current density for diffusion-controlled stability of electrolytic surface nanobubbles. *Proc. Natl Acad. Sci. USA* **121** (21), e2321958121.

https://doi.org/10.1017/jfm.2025.10760 Published online by Cambridge University Press